Energy Advances

ROYAL SOCIETY OF CHEMISTRY

PAPER

View Article Online
View Journal | View Issue

Check for updates

Cite this: *Energy Adv.*, 2024, 3, 883

Carbon fiber composite electrodes derived from metal organic polyhedra-18 and matrimid for hybrid supercapacitors†

Syed Fahad Bin Haque, Yafen Tian, Daniel W. Tague, Kenneth J. Balkus Jr. and John P. Ferraris*

Received 5th November 2023,
Accepted 22nd March 2024

DOI: 10.1039/d3ya00537b

rsc.li/energy-advances

Matrimid and metal–organic polyhedra–18 (MOP-18) electrospun composite nanofibers were utilized to fabricate free-standing, electrically conducting, and high-energy density hybrid supercapacitor electrodes. Electrospinning multiple compositions of Matrimid and MOP-18 mixture followed by carbonization and activation with CO_2 resulted in C/Cu/Cu_2O nanocomposite fibers that exhibited an energy density of up to 12.69 W h kg^{-1} and a specific capacitance of 253.4 F g^{-1} at 1 A g^{-1} current density in 6 M KOH electrolyte. The high energy density of the material can be attributed to the uniform dispersion of redox-active metal/metal oxide particles facilitated by the high solubility of the MOP-18 precursor. The thermal decomposition of MOP-18 during carbonization produced volatile species that increase the surface area and porosity of the resultant carbon allowing for better access of electrolyte ions during charging/discharging. Furthermore, MOP-18 carbonization lowered the I_D/I_G of the composite electrodes, consistent with increased graphitization.

Introduction

The need for efficient and cost-effective electrical energy storage systems is projected to increase in the near future as a result of a shift toward renewable energy and electric transportation.[1,2] A synergistic combination of electrochemical double-layer capacitors (EDLC) and pseudocapacitors (PC) known as hybrid supercapacitors promises to be a viable alternative for current and future energy storage needs. They are relatively safe, low-cost, long-lasting, and sustainable electrical energy storage systems compared to other available methods.[3–5] Li-ion batteries, currently the most widely used energy storage for consumer electronics and electric vehicles, have been significantly improved in recent years, particularly in terms of energy density and associated cost.[6–9] Nevertheless, the operating temperature range, low power density, relatively short cyclability, and significant fire hazard compared to other storage methods have inspired efforts to develop alternatives.[10–13] EDLCs have been studied for this purpose as they have higher power density and longer cycle life compared to Li-ion batteries but their energy density is lower by several orders of magnitude.[14–18] PCs based on conducting polymers and redox-active metal oxides have also been studied because they have better energy density than EDLCs. However, PCs have poor cyclability or low electrical conductivity which limits their utility.[16,19–22] Hybrid supercapacitors have the potential to bring a well-balanced synergistic combination of both EDLC and pseudocapacitors to simultaneously afford superior energy density, power density, and cyclability.[23–29]

Hybrid supercapacitor electrodes generally consist of a composite/physical mixture of carbon-based EDLC components along with a metal/metal oxide or conducting polymer pseudocapacitive component.[30–35] The EDLC part of the electrode mainly contributes conductivity and power density while pseudocapacitive materials add energy density.[4] Combining EDLCs and PCs in a way that enhances the other is the major challenge in designing hybrid supercapacitor electrodes. The interface between these two components plays an important role in dictating the performance and usability of the electrode material.[36] Redox-active pseudocapacitive materials need high effective surface area, access to the electrolyte, and sufficient electrical conductivity to perform at full potential.[37] A physical mixture of carbon and redox-active materials often fails to provide the redox-active species with all these necessities. Special structures like core–shell, 1D and 2D hybrids, intimate contact composites, and superior mixing techniques like *in situ* dispersion are necessary for both components to work efficiently and effectively.[38–41]

Numerous metal nanoparticles and metal oxides including copper have been incorporated into hybrid supercapacitors to

---

Department of Chemistry and Biochemistry, The University of Texas at Dallas, Richardson, TX 75080-3021, USA. E-mail: ferraris@utdallas.edu

† Electronic supplementary information (ESI) available. See DOI: **https://doi.org/10.1039/d3ya00537b**

improve energy density.[42–46] The problem of dispersion of redox particles, control of particle size, and prevention of side reactions like crosslinking between carbon and metal phases has slowed the advancement of this approach. Additionally, the introduction of redox particles often reduces the available surface area of the carbon counterpart which hinders overall performance. To achieve high energy density through pseudocapacitance in carbon-based supercapacitor electrodes CuO,[47–49] CuS,[50] and other copper compounds and complexes have been previously studied.[51,52] The difficulty of controlling particle size, especially for copper metal nanoparticles, dispersion, and integration of redox-active species has limited the desired outcome from these electrode systems. Often metal–organic frameworks (MOF) have been studied to solve this issue, but MOFs lack solubility for uniform particle dispersion.[53] Metal–organic polyhedra (MOP) with long carbon chains attached to their outer shell are soluble in organic solvents and hence they can be utilized to disperse redox active metal nanoparticles.[54] Additionally, thermal decomposition of MOP structures creates porosity in the electrode enhancing the surface area and electrolyte accessibility after carbonization. Metal–organic polyhedra-18 (MOP-18) was used in this study as a PC precursor and to the best of our knowledge, this work presents the first hybrid supercapacitor based on a metal–organic polyhedra derived PC component. In the outer shell, MOP-18 contains 24 dodecyl alkane chains, and in the inner core, it consists of 24 copper atoms in 12 paddle-wheel units.[55,56] The long carbon chains attached to the structure render MOP-18 highly soluble in a variety of organic solvents which aided mixing with Matrimid polymer during electrospinning. MOP-18 was uniformly dispersed in the composite nanofiber, which afforded small copper and copper oxide nanoparticles after carbonization. The metal–organic structure of MOP-18 ensured a composite of Cu/Cu_2O with low internal resistance. While carbonizing the electrode, the MOP-18 structure decomposed to introduce micropores which increased the electrolyte accessibility of the redox particle as well. The carbonized and CO_2 activated composite of Matrimid and MOP-18 at a current density of 1 A g^{-1} delivers a specific capacitance of 253.3 F g^{-1} and an energy density of 12.69 W h kg^{-1} in a 6 M KOH electrolyte solution.

Experimental

Materials

Matrimid 5218 was sourced and used without further purification from Ciba Specialty Chemicals. Potassium hydroxide was purchased from Fisher Scientific. Sodium bicarbonate, 5-hydroxyisophthalic acid, 1-iodododecane, ethyl acetate, acetonitrile, methanol, copper acetate monohydrate, tetrachloroethane, and chloroform for MOP-18 synthesis were purchased and used without farther purification from Sigma-Aldrich with more than 97% purity. Dimethylformamide (DMF) and dimethylacetamide (DMAc) solvents of 99.8% purity were purchased from Sigma-Aldrich and Millipore Corporation, respectively.

MOP-18 synthesis

A published procedure was used to synthesize MOP-18.[55] 5-Dodecoxyisophthalic acid, the linker for MOP-18 synthesis was prepared by esterification of 5-hydroxyisophthalic with ethanol, alkylating the diester's hydroxyl group followed by hydrolysis. 2.7 g of the synthesized linker were dissolved in 100 mL of DMF at 80 °C while stirring until the solution was clear. 1.5 g of copper acetate was dissolved at room temperature in 50 mL of DMF. The two solutions were mixed, and 100 mL of methanol was added to initiate precipitation. The solid precipitate was left to crystallize for 24 h at room temperature and then washed repeatedly with methanol at room temperature.[56] The blue solid was dried at 60 °C for 24 h. The product MOP-18 crystals were characterized by powder XRD (Fig. S1, ESI†).

MOP-18 and matrimid fiber preparation

Matrimid (0.6 g) was dissolved in 3.63 mL of DMAc at room temperature to produce a 15% solution by weight. Separate solutions of MOP-18 were prepared by dissolving 0.3 g, 0.6 g, and 1.2 g of MOP-18 in 1.7 mL, 3.4 mL, and 6.8 mL of DMAc respectively at room temperature to obtain a 15 wt% solution of MOP-18. Then the Matrimid solution and MOP-18 solution were mixed to produce 2 : 1, 1 : 1, and 1 : 2 dry w/w ratios of Matrimid/MOP-18. The mixtures were stirred for 24 hours at room temperature to ensure uniformity. The resulting solution was then electrospun using a custom-built electrospinning setup. The uniformly mixed polymer solution was charged at a rate of 0.5 mL h^{-1}. The 20 Ga blunt tip needle connected to the 10 mL syringe had a positive potential of 20 kV and had a translation motion during spinning. A rotating collecting drum covered with aluminium foil had a negative potential of 5 kV and was rotated at 300 rpm. The distance between the needle tip to the collector was maintained at 15 cm. As-spun fibers were collected and dried under vacuum at 150 °C for 24 h. To carbonize and activate the e-spun fibers, the mat was heated at 800 °C using a 5 °C min^{-1} heating rate and held there for 60 min under a constant N_2(g) flow rate of 200 SCCM. Then CO_2(g) was passed over the fibers for an additional 30 min at 800 °C in a 3 : 1 N_2 to CO_2 ratio at a constant flow rate of 240 SCCM to activate the fibers (Fig. 1).

Characterization

Numerous characterization techniques were utilized to understand the physical structure and electrochemical performance of the synthesized Matrimid/MOP-18 hybrid electrodes. The Powder X-ray diffraction patterns were collected using a Rigaku Ultima IV diffractometer (Cu Kα radiation). A Thermo Scientific DXR Raman microscope with a laser excitation wavelength of 532 nm was used to obtain the Raman spectra. X-ray photoelectron spectroscopy (XPS) measurements using a PHI Versa Probe II determined the composition of the surface elements. A monochromatic Al Kα radiation ($h\nu$ = 1486.6 eV) was used to generate the photoelectrons and the spectra were collected in a hemispherical analyzer at 0.2 eV step size and a pass energy of 11 eV for survey and 23.5 eV for analysis. Fiber morphology

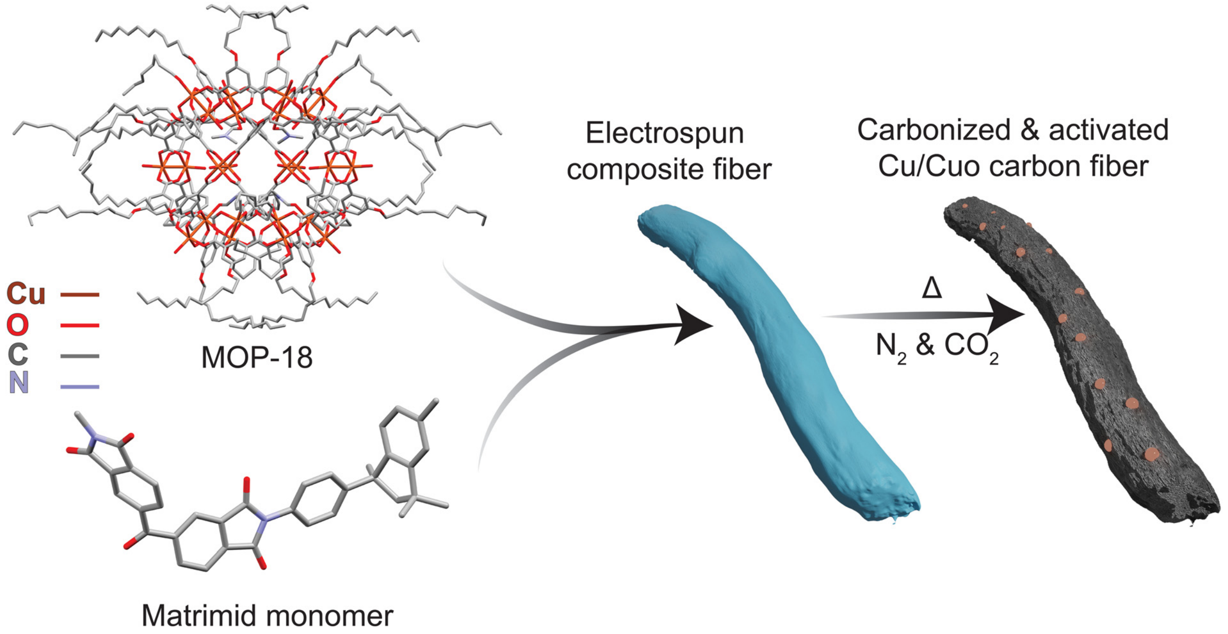

Fig. 1 Schematic illustration showing the preparation process of Cu/CuO carbon fiber composite.

after carbonization and activation was characterized by high-resolution transmission electron microscopy (HRTEM) JEOL JEM-2100 TEM at 200 kV. A Zeiss SUPRA 40 SEM instrument was used to collect micrographs of carbonized samples. Micromeritics ASAP 2020 was used to collect nitrogen and carbon dioxide adsorption–desorption isotherms at 77 K and 273 K respectively. The Brunauer–Emmett–Teller (BET) method was used to determine the specific surface area after carbonization and activation. The two-dimensional nonlinear density functional theory (2D NLDFT) method was used to determine the

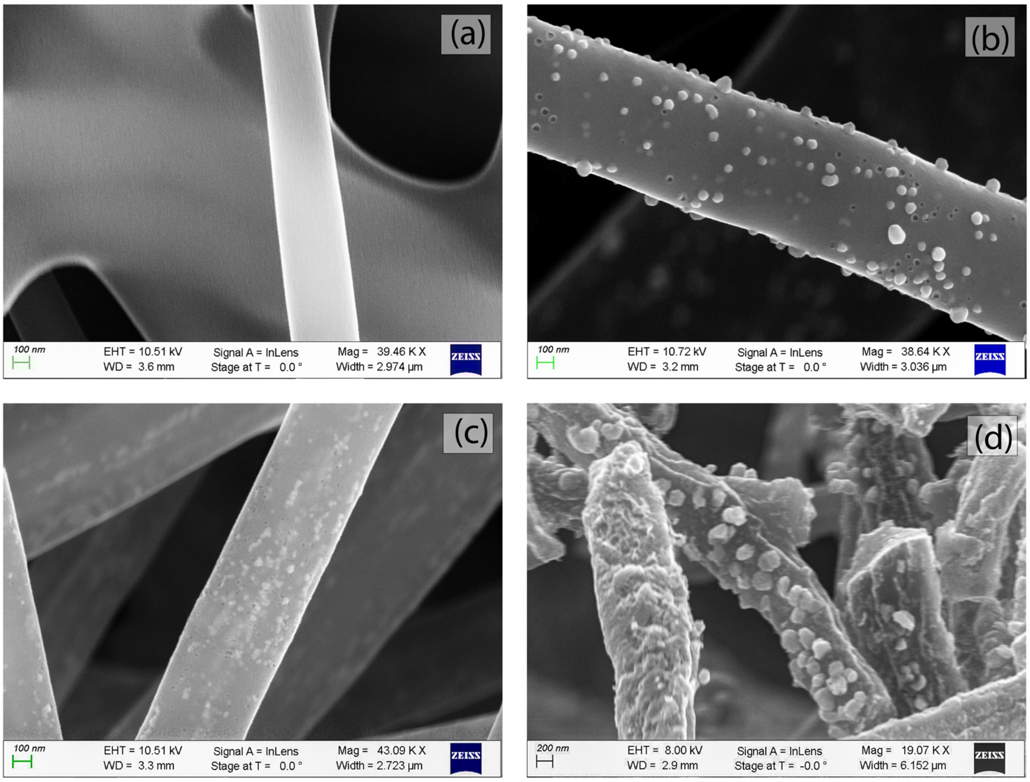

Fig. 2 SEM images of carbonized fiber from (a) Matrimid (b) 2 : 1 Matrimid/MOP-18 (c) 1 : 1 Matrimid/MOP-18 and (d) 1 : 2 Matrimid/MOP-18.

pore size distribution from the gas adsorption–desorption isotherm.[57] The conductivity of carbonized and activated composite electrode materials was measured using a DP03 Alessi 4-point probe instrument paired with a QuadTech LR2000 digital milliohmmeter.

Results and discussion

The SEM images in Fig. 2 show the Matrimid/MOP-18 composite fibers after carbonization and activation. Carbonized Matrimid fibers in Fig. 2(a) have a relatively smooth surface with an average diameter of about 300 nm. Copper nanoparticles are visible in Fig. 2(b–d) on the surface of the carbonized fibers that contained MOP-18. Upon carbonization, MOP-18 decomposes, producing metallic copper particles. During CO_2 activation the trace amounts of oxidizing gases produced from decomposing polymer chains create an oxide layer on a portion of the particles preventing their melting and recrystallization. On the other hand, unoxidized particles undergo Ostwald ripening during the high-temperature carbonization process and grow. The 2 : 1 Matrimid/MOP-18 composite in Fig. 2(b) shows a particle-decorated carbon fiber that has a fiber diameter of around 400 nm with particles on the surface that are around 100 nm. Additionally, from SEM of 1 : 1 and 1 : 2 Matrimid/MOP-18 samples in Fig. 2(c) and (d) respectively, redox-active copper and copper(I) oxide particles are visible indicating electrolyte accessibility.

The TEM images in Fig. 3 of carbonized composite fibers show a bimodal distribution of Cu and Cu_2O particles. A histogram of particle size distribution is also presented in the ESI† in Fig. S3. More than 80% of the particles are 5–20 nm in size among which more than 60% are 10–15 nm. Particles greater than 40 nm in size account for less than 2%. All three carbonized fibers of varying composition in Fig. 3 show that both sets of particles are well dispersed in carbon.

HRTEM images of carbonized 1 : 1 Matrimid/MOP-18 composites are shown in Fig. 4(a–c). The presence of particles ranging from 10 nm in diameter to 100 nm with their corresponding lattice fringes is visible in the HRTEM images. The d-spacing of 0.38 nm of carbon (002) plane in Fig. 4(a) shows the graphite has a slightly expanded interlayer spacing due to the presence of turbostratic disorder.[58] Additionally, the d-spacing of 0.21 nm of copper (111) plane and 0.24 nm of copper(I) oxide (111) plane is visible from HRTEM images in Fig. 4(b) and (c) respectively.[59,60] HRTEM reveals the presence of both copper and copper(I) oxide particles in the system with an indication of particles close to 10 nm in size predominantly being copper(I) oxide.

The X-ray diffraction (XRD) patterns of the carbonized Matrimid/MOP-18 composites show peaks associated with both Cu and Cu_2O after carbonization and activation at 800 °C. Fig. 5 shows copper metal particles exhibiting peaks at 43.5°, 50.4°,

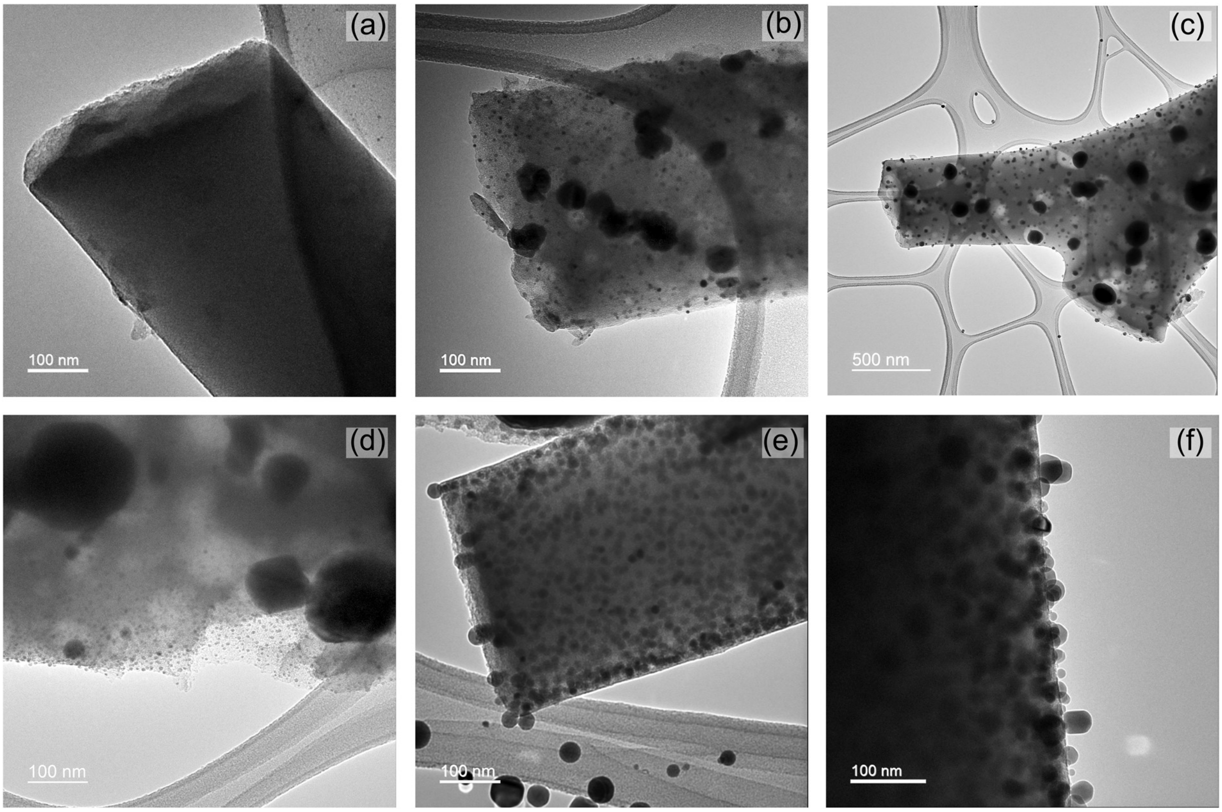

Fig. 3 TEM images of carbonized fiber from (a) Matrimid (b) 2 : 1 Matrimid/MOP-18 (c) and (d) 1 : 1 Matrimid/MOP-18 and (e) and (f) 1 : 2 Matrimid/MOP-18.

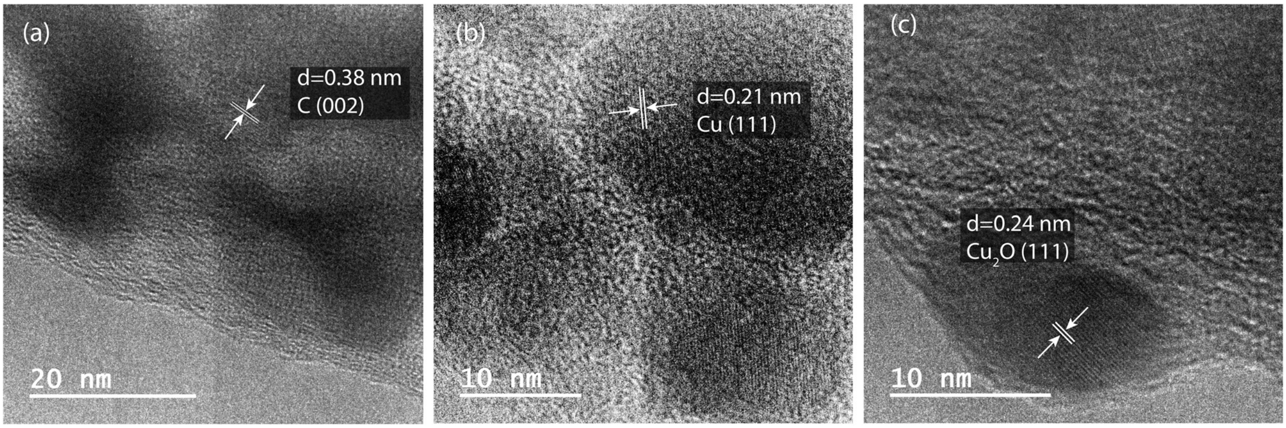

Fig. 4 (a)–(c) HRTEM images of carbonized 1 : 1 Matrimid/MOP-18.

and 74.2° which are associated with the (111), (200), and (220) planes (JCPDS No. 003–1018).[61] For the Cu_2O crystals, peaks shown at 36.3°, 42.4°, and 61.6° correspond to the (111), (200), and (220) peaks (JCPDS No. 05-0667).[62] Partially crystalline carbon exhibited a broad peak around 24° corresponding to the (002) plane of graphene which is slightly shifted from the ideal graphite peak at 26.1° due to a turbostratic disorder.[63,64] Peaks associated with Cu_2O are significantly broader than peaks associated with Cu planes indicating oxide particles are smaller than metal particles.

Raman spectroscopy was used to characterize the carbon component after the carbonization and activation procedure. Fig. 6 shows the fitted Raman spectrum of the carbon fibers obtained from 1 : 1 Matrimid/MOP-18. The D1-band at 1350 cm^{-1} is associated with amorphous carbon materials and G-band at 1580 cm^{-1} represents graphitized carbon.[65] The Raman spectra are deconvoluted into D1, D3, D4, and G band.[66] Sp2–sp3 carbon bonds are represented by the D4 peak in the 1180–1290 region. The D3 peak is associated with the semicircle stretch of benzene rings in amorphous carbon.[67] The deconvoluted I_D/I_G ratio by height is a representation of the degree of graphitization and is related to the conductivity of synthesized carbon. I_D/I_G ratios of carbonized and activated 2 : 1, 1 : 1, and 1 : 2 Matrimid/MOP-18 were 0.9, 0.78, and 0.86, respectively (Fig. S5 and S6, ESI†) whereas carbonized and activated Matrimid has an I_D/I_G ratio of 1.1 (Fig. S4, ESI†) which indicates enhanced graphitization due to the catalytic effect of present copper nanoparticles.[68,69]

Fig. 7(a) shows the deconvoluted XPS spectra of carbon in the carbonized 1 : 1 Matrimid/MOP-18 composite. Peaks appear at 284.5, 285.2, 286.3, 288.4, and 291 eV representing C═C, C–C, C–O–C, C═O, and the carbon π–π* satellite, respectively. The presence of the π–π* satellite peak indicates electrically conducting graphitic carbon materials as it arises from delocalized π-bond electrons. XPS spectra of copper show the presence of copper (0) and copper (I) $2p_{3/2}$ and $2p_{1/2}$ peaks at 932.6 and 952.5 eV.[61,70,71] The absence of any strong satellite peak indicates that no CuO is present in the system.[72]

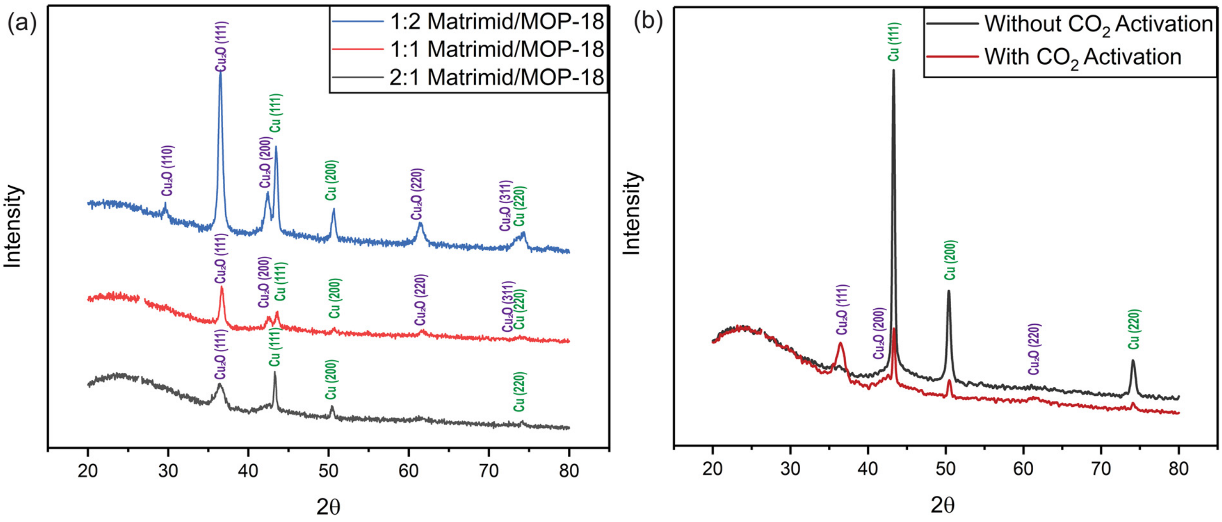

Fig. 5 (a) XRD of carbonized and activated fiber from Matrimid/MOP-18 composites. (b) XRD pattern of CO_2 activated and non-activated 1 : 1 carbonized Matrimid/MOP-18.

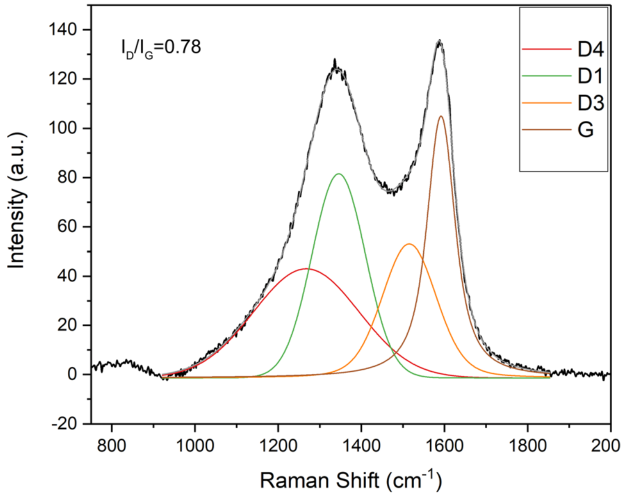

Fig. 6 Raman spectrum of 1 : 1 Matrimid/MOP-18 after carbonization at 800 °C.

Fig. 8(a) shows the N_2 adsorption–desorption isotherm of carbonized Matrimid and three Matrimid/MOP-18 composites. The isotherms show a type IV hysteresis with substantial gas adsorption in the low-pressure region indicating the presence of both mesopores and micropores. The CO_2 adsorption isotherm was also collected for all the samples as shown in ESI† Fig. S7. The corresponding pore size distribution obtained by the 2D NLDFT method combining both the N_2 and CO_2 adsorption–desorption isotherms is shown in Fig. 8(b). There is mesoporosity in the samples but most of the porosity for all the composites lies in the microporous region (≤20 Å). The specific surface area of carbonized and activated Matrimid was found to be 377 m^2 g^{-1} which increased with the addition of MOP-18 to 444 m^2 g^{-1} in the case of 1 : 1 Matrimid/MOP-18. The surface area of the electrode materials increased after adding MOP-18 due to porosity generated by the decomposition of MOP-18 at high temperatures.[56,73–75] The surface areas for 2 : 1 and 1 : 2 carbonized and activated Matrimid/MOP-18 were 268 m^2 g^{-1} and 564 m^2 g^{-1}, respectively. Fig. 8(b) shows the total amount of microporosity increases with the increasing amount of MOP-18 in the composite. The pore size distribution shows a set of pores at 3.8 Å and another set of pores at 5.6 Å. Carbonized Matrimid had the smallest amount of porosity at 3.8 Å and did not have any at 5.6 Å. The increase in the surface area and microporosity demonstrates the benefit of adding redox particles in the form of metal–organic polyhedral precursors. The pore sizes and distribution in the synthesized composites are compatible with the smaller sized electrolyte ions present in aqueous KOH solution.[76]

Fig. 9 shows the thermogravimetric analysis (TGA) of Matrimid and Matrimid/MOP-18 composites fibers under nitrogen gas. MOP-18 starts to degrade around 300 °C and Matrimid starts to lose mass around 450 °C. Matrimid carbonizes completely before 900 °C after losing 45% of its mass. As MOP-18 loses about 80% of its mass before reaching 500 °C, the char yield of composite fibers is less than Matrimid-only fibers. The carbonized mass of the composite fibers is 55%, 42%, 39%, and 33.5% of the original mass of Matrimid and 2 : 1, 1 : 1, and 1 : 2 Matrimid/MOP composite fibers, respectively after heating them to 800 °C under N_2.

All the electrode materials are characterized in electrochemical tests by fabricating T-cells where Matrimid/MOP-18 composite electrode materials are used as a working electrode. A carbonized and CO_2-activated 4 : 1 PAN/PMMA fiber mat was used as the counter electrode to fabricate asymmetric cells. 6 M KOH was used as an electrolyte and a PTFE membrane was used as the separator during cell fabrication. Fig. 10 shows that the 1 : 1 Matrimid/MOP-18 shows the highest energy density *versus* power density. Carbonized Matrimid shows the lowest

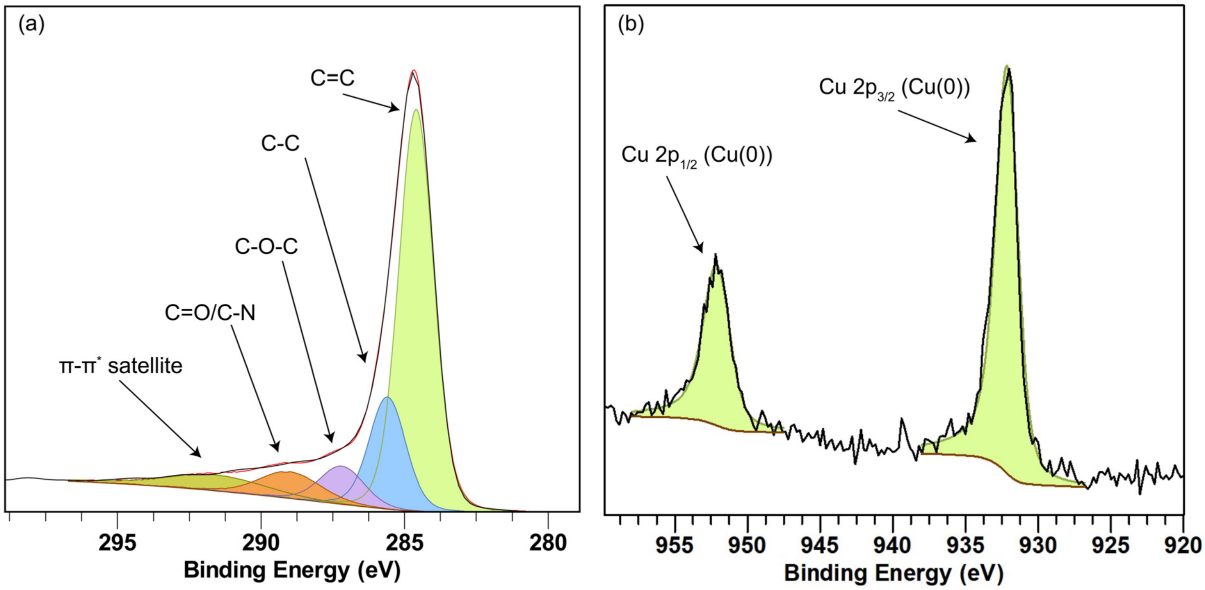

Fig. 7 XPS spectra of carbon (a) and copper (b) present in carbonized 1 : 1 Matrimid/MOP-18 composite.

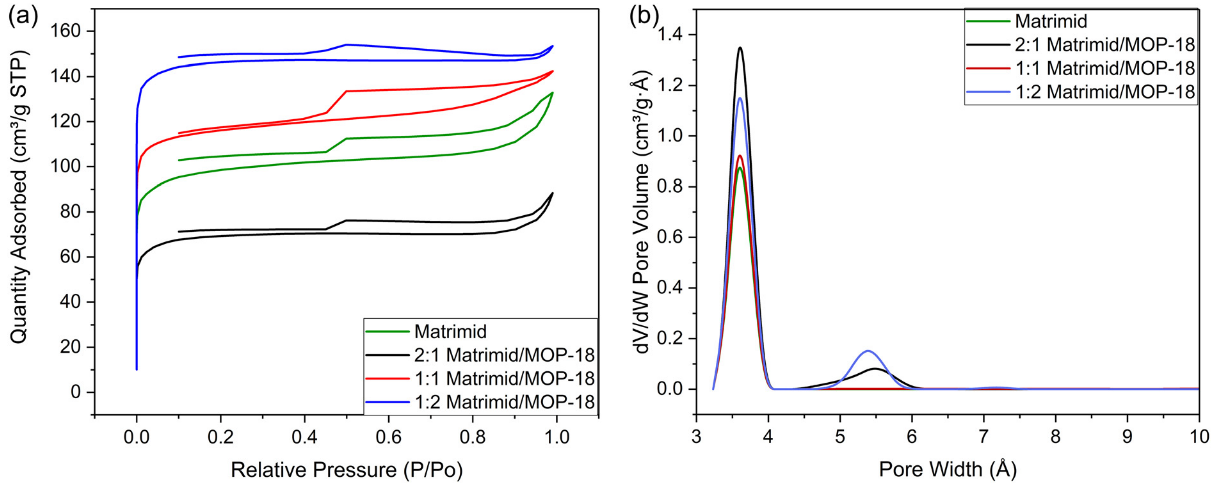

Fig. 8 (a) N_2 adsorption–desorption isotherm and (b) pore size distribution of synthesized Matrimid and Matrimid/MOP-18 carbonized fibers.

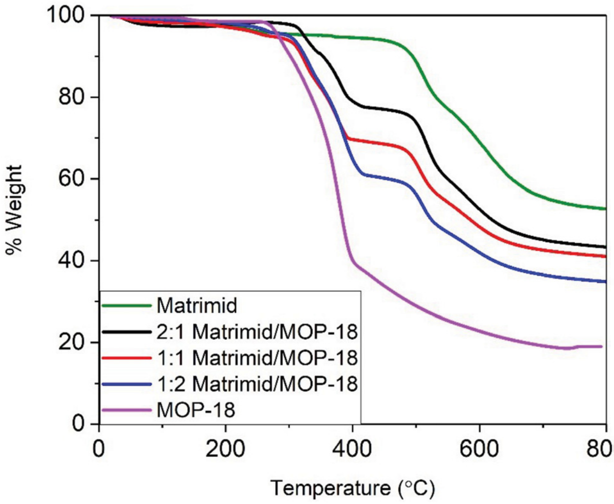

Fig. 9 Thermogravimetric analysis of Matrimid and Matrimid/MOP-18 composite fibers under nitrogen.

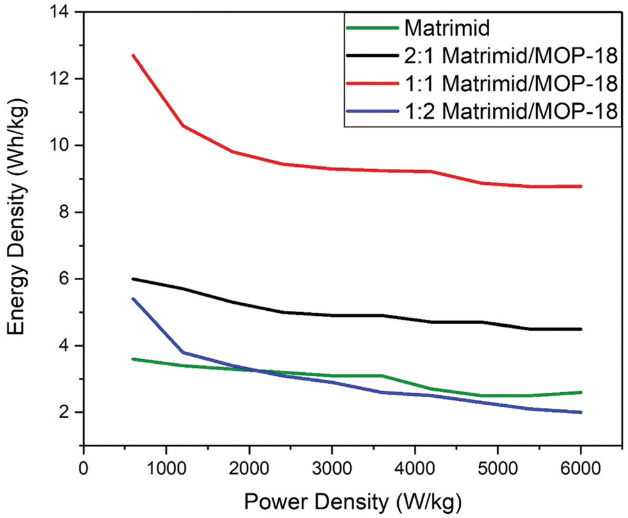

Fig. 10 Power density vs energy density graph from two electrode galvanostatic charge–discharge experiment of carbonized and activated Matrimid and 2 : 1, 1 : 1 and 1 : 2 Matrimid/MOP-18 composites.

performance among all the composites in most test conditions except 1 : 2 Matrimid/MOP-18 composite at higher power density.

Fig. 11(a) shows multiple scanning starting from a potential of −1 V to a higher potential of 0 V to 0.5 V successively in a three-electrode setup where the reference electrode is Ag/AgCl in a saturated KCl solution. The purpose of the study was to find where the redox activity occurs and how many oxidation-state changes the redox-active particles are going through during each cycle. It shows the neutral copper particles oxidize to a (+1) oxidation state at −0.3 V and further oxidize to a (+2) oxidation state at 0.15 V. During the reversed cycling potential, the particles reduce back to (+1) at a voltage of −0.3 V and further reduce to an oxidation state of (0) at −0.65 V. Metal particles go through these successive faradaic transitions according to the mechanism presented in reference No. 55.[77,78]

Fig. 11(b) shows a two-electrode cyclic voltammogram of 1 : 1 Matrimid/MOP-18 at scan rates of 10, 25, 50, and 75 mV s^{-1}. The voltammograms display a nearly box-like shape overlaid with broad peaks from redox activity. Three-electrode cyclic voltammogram in Fig. 11(a) shows the redox active particles present in the electrode participate in faradaic reaction at a negative potential *vs.* Ag/AgCl reference electrode. Hence, the redox-active working electrode is used as the negative electrode in the experiment, and a mostly negative potential window is chosen to allow them to contribute to the current response.[79] Since peaks resulting from redox activity visible in the CVs complicate the calculation of capacitance, energy density, and power density, galvanostatic charge–discharge experiments were utilized to calculate these performance metrics.

Fig. 11(c) shows a 2-electrode galvanostatic charge–discharge (GCD) of 1 : 1 Matrimid/MOP-18 from 1–10 A g^{-1} current

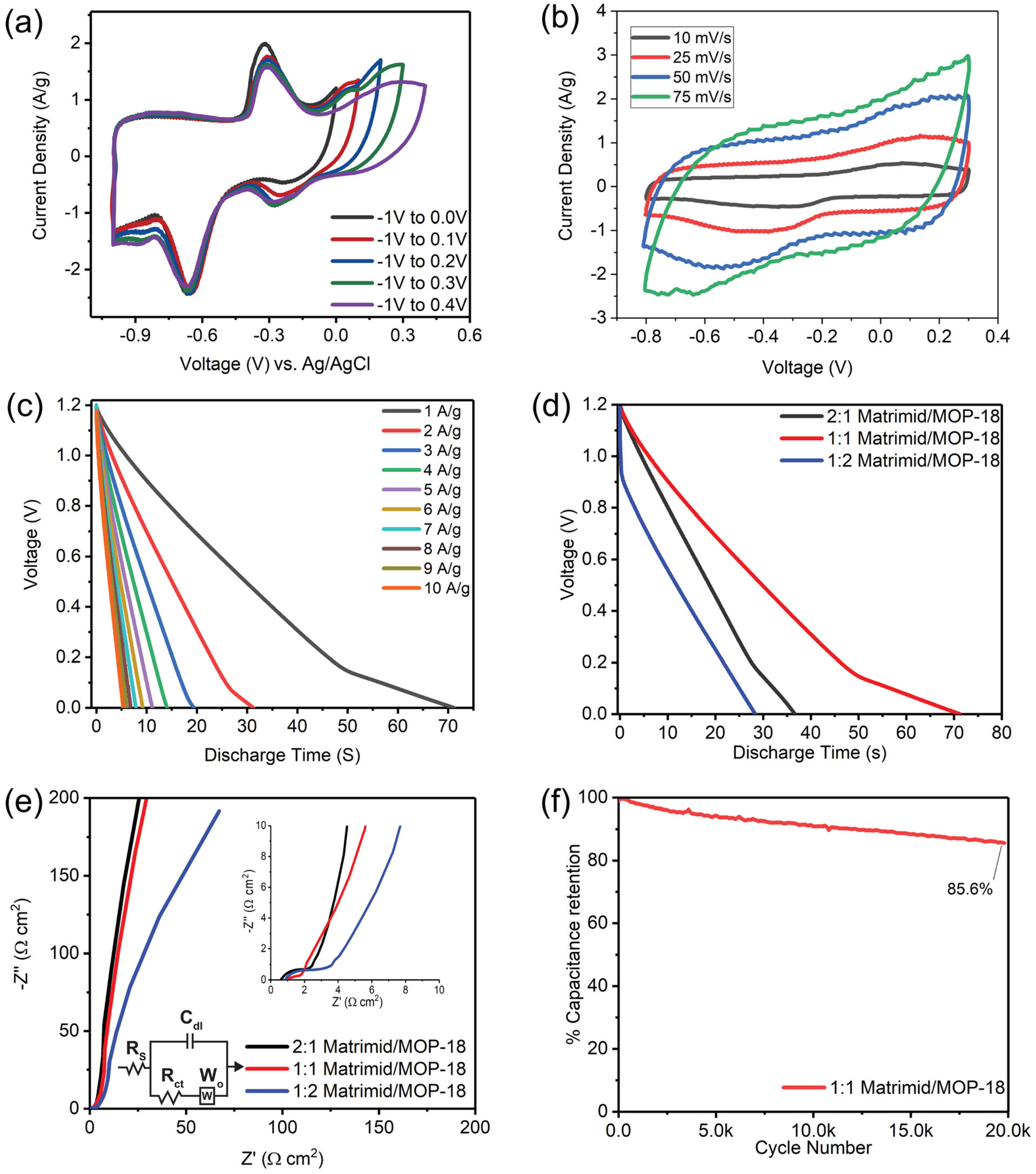

Fig. 11 (a) Scanning of redox activity of 1 : 1 Matrimid/MOP-18 composite at 5 mV s^{-1} from −1 V to 0 V, 0.1 V, 0.2 V, 0.3 V, 0.4 V, and 0.5 V against Ag/AgCl reference electrode. (b) Cyclic voltammetry (2-electrode) at 10, 25, 50, and 75 mV s^{-1} scan rate of 1 : 1 Matrimid/MOP-18. (c) Galvanostatic charge–discharge of 1 : 1 Matrimid/MOP-18. (d) Galvanostatic charge–discharge comparison of 2 : 1, 1 : 1 and 1 : 2 Matrimid/MOP-18 at 1 A g^{-1} current density. (e) Electrochemical impedance spectroscopy of 2 : 1, 1 : 1 and 1 : 2 Matrimid/MOP-18 (f) Cyclability test of 1 : 1 Matrimid/MOP-18 composite electrode in 6 M KOH electrolyte at 5 A g^{-1} current density.

density. The working electrode was used as a negative electrode in an asymmetric cell to allow redox reactions in the negative potential region evident from CV. The GCD shows deviation from linearity caused by redox activity at low current density in the low voltage region. Voltage drop in the GCD is relatively low compared to other reported copper metal and oxide and carbon-based electrodes except 1 : 2 carbonized Matrimid/MOP-18 composite.[80,81]

Fig. 11(d) shows a comparison of galvanostatic discharge between all three composites at 1 A g^{-1} current density. From this study, it is seen that the 1 : 1 Matrimid/MOP-18 composite holds the most amount of charge at this current density, taking

Table 1 Electrochemical performance comparison of carbonized 1 : 1 Matrimid/MOP-18 supercapacitor electrodes with other reported studies

Material	Electrolyte	Specific capacitance	Voltage window	Energy density (W h kg^{-1})	Power density (W kg^{-1})	Cyclic stability	Ref.
ZIF-8/PAN	PVA: 1 M H_2SO_4	64.0 F g^{-1} at 1 A g^{-1}	0–1.0	7.9	219	90% (10 000)	82
ZIF-8, BDBA	6 M KOH	242 F g^{-1} at 1 A g^{-1}	0–1.0	8.4	500	99.7% (8000)	83
CNF/Ni-CAT	2 M KOH	68.58 F g^{-1} at 0.5 A g^{-1}	0–1.4	18.67	297.12	106% (5000)	84
ZIF-67/thiourea	PVA: 1 M H_2SO_4	103 F g^{-1} at 0.5 A g^{-1}	0–1.0	14.3	250	107% (3000)	85
Co_3O_4	2 M KOH	150 F g at 1 A g^{-1}	0–0.5	—	—	106% (3000)	86
MOP-18/CNF	6 M KOH	253.4 F g^{-1} at 1 A g^{-1}	0–1.2	12.69	600	85.6% (20 000)	This work

the longest time to discharge from 1.2 V to 0 V at 1 A g^{-1} current density. The 2 : 1 Matrimid/MOP-18 discharges twice as fast since it does not have as much redox capability as the 1 : 1 composite. Even though the 1 : 2 Matrimid/MOP-18 should have the highest amount of redox capability, its high impedance visible from EIS limits its electrochemical performance.

Its higher resistance is also evident from the IR drop visible in the galvanostatic charge–discharge experiment. At 1 A g^{-1}, the 1 : 1 Matrimid/MOP-18 composite shows a specific capacitance of 253.3 F g^{-1}, an energy density of 12.69 W h kg^{-1}, and a power density of 600 W kg^{-1}. 1 : 2 Matrimid/MOP-18 composite however at the same condition shows a capacitance of 108.2 F g^{-1} and an energy density of 5.4 at a power density of 600 W kg^{-1}. 2 : 1 Matrimid/MOP-18, on the other hand, shows a specific capacitance of 120.5 F g^{-1} and an energy density of 6 W h kg^{-1} at a power density of 600 W kg^{-1}.

Electrochemical impedance spectroscopy (EIS) overlays of all three composites are shown in Fig. 11(e) from 100 kHz to 0.01 Hz frequency with a focused high-frequency region in the inset. The Randles Cell circuit model was employed to fit the impedance spectra of the electrode composites, incorporating an equivalent resistance or solution resistance (R_s), a double-layer capacitor (C_{dl}), a charge-transfer resistance (R_{ct}) which is proportional to the diameter of the semicircle at the intermediate frequency region on a Nyquist plot, and a Warburg component, which represents the diffusion driven impedance for faradaic processes. The R_s, C_{dl}, and R_{ct} values of all three carbonized and activated Matrimid/MOP-18 composites are given in Table 2.

The 1 : 1 Matrimid/MOP-18 composite exhibited the smallest semicircle on the Nyquist plot and had the lowest R_{ct} value. In contrast, the 1 : 2 Matrimid/MOP-18 composite demonstrated both the highest R_s and R_{ct} values. Consequently, despite having the highest relative amounts of redox-active particles by mass, its performance was inferior to the 1 : 1 Matrimid/MOP-18 composite. This observation underscores the importance of optimizing the ratio of components in the composite to achieve superior performance.

Table 2 Equivalent resistance, capacitance, and charge transfer resistance of carbonized and activated Matrimid/MOP-18 composites from impedance spectroscopy

	2 : 1 Matrimid/ MOP-18	1 : 1 Matrimid/ MOP-18	1 : 2 Matrimid/ MOP-18
R_s	0.43445	0.69	0.98
C_{dl}	2.86×10^{-6}	6.02×10^{-5}	5.83×10^{-6}
R_{ct}	0.81955	0.27571	1.32158

Fig. 11(f) shows capacitance retention with cycle numbers for the 1 : 1 Matrimid/MOP-18 composite. The experiment was done at 5 A g^{-1} current density and the cell was charged and discharged between 1.2 V to 0.6 V repeatedly. The cycling stability test shows the 1 : 1 composite has a retention of more than 85% capacitance after 20 000 cycles. The electrode material shows higher cyclability compared to relevant other studies referred to here.[69,80,81,87] A comparison of electrochemical performance metrics between previously reported similar composite electrodes and those of this work for hybrid supercapacitors is presented in Table 1.[88,89] Two-electrode and three-electrode cyclic voltammograms and galvanostatic charge–discharge plots of studied composites and Matrimid electrodes after carbonization and activation are also presented in Fig. S9–S15 with performance metrics in Tables S1–S4 (ESI†).

Conclusions

In summary, C/Cu/Cu_2O nanofiber composites were synthesized by electrospinning and carbonizing Matrimid/MOP-18 solutions. CO_2 activation was used to increase the surface area of synthesized electrode materials. Using MOP-18 instead of other copper precursors helped to ensure uniform dispersion of nanoparticles of small dimensions. This aided in the enhanced utilization of present redox particles in the electrode materials. Also, MOP-18 helped to improve the surface area of the composite as its thermal decomposition introduces pores in the composite for better electrolyte accessibility. The energy density of 12.69 W h kg^{-1} at a current density of 1 A g^{-1} was achieved in the study in a 6 M KOH electrolyte. The method used in the study successfully illustrates the potential of materials like metal–organic polyhedra as precursors for redox-active particles to be used in electrical energy storage.

Author contributions

Formal analysis, investigation, methodology software, visualization and writing – original draft, Syed Fahad Bin Haque. Conceptualization, data curation, project administration, resources, supervision and writing – review and editing, John P. Ferraris, Kenneth J. Balkus Jr; formal analysis, Yafen Tian and Daniel W. Tague.

Conflicts of interest

The authors disclose that they have no conflicting financial interests.

References

1 P. Simon and Y. Gogotsi, *Nat. Mater.*, 2020, **19**, 1151–1163.

2 H. Sun, Y. Zhang, J. Zhang, X. Sun and H. Peng, *Nat. Rev. Mater.*, 2017, **2**, 1–12.

3 M. F. El-Kady, Y. Shao and R. B. Kaner, *Nat. Rev. Mater.*, 2016, **1**, 1–14.

4 L. Kouchachvili, W. Yaïci and E. Entchev, *J. Power Sources*, 2018, **374**, 237–248.

5 M. P. Down, S. J. Rowley-Neale, G. C. Smith and C. E. Banks, *ACS Appl. Energy Mater.*, 2018, **1**, 707–714.

6 S. Goriparti, E. Miele, F. De Angelis, E. Di Fabrizio, R. P. Zaccaria and C. Capiglia, *J. Power Sources*, 2014, **257**, 421–443.

7 M. Wakihara, *Mater. Sci. Eng., R*, 2001, **33**, 109–134.

8 K. Striebel, J. Shim, A. Sierra, H. Yang, X. Song, R. Kostecki and K. McCarthy, *J. Power Sources*, 2005, **146**, 33–38.

9 L. Yaqoob, T. Noor and N. Iqbal, *ACS Omega*, 2022, **7**, 13403–13435.

10 Z. Yu, H. Shan, Y. Zhong, X. Zhang and G. Hong, *ACS Energy Lett.*, 2022, 3151–3176.

11 P. Simon, Y. Gogotsi and B. Dunn, *Science*, 2014, **343**, 1210–1211.

12 V.-P. Vu, V.-D. Mai, D. C. T. Nguyen and S.-H. Lee, *ACS Appl. Energy Mater.*, 2022, **5**, 2211–2220.

13 P. G. Campbell, M. D. Merrill, B. C. Wood, E. Montalvo, M. A. Worsley, T. F. Baumann and J. Biener, *J. Mater. Chem. A*, 2014, **2**, 17764–17770.

14 H. Shao, Y. C. Wu, Z. Lin, P. L. Taberna and P. Simon, *Chem. Soc. Rev.*, 2020, **49**, 3005–3039.

15 Y. A. Maletin, N. G. Stryzhakova, S. O. Zelinskyi and S. I. Chernukhin, *Theor. Exp. Chem.*, 2022, 1–14.

16 A. Muzaffar, M. B. Ahamed, K. Deshmukh and J. Thirumalai, *Renewable Sustainable Energy Rev.*, 2019, **101**, 123–145.

17 E. Adhamash, R. Pathak, Q. Qiao, Y. Zhou and R. McTaggart, *RSC Adv.*, 2020, **10**, 29910–29917.

18 Z. Ayaganov, V. Pavlenko, S. F. Bin Haque, A. Tanybayeva, J. Ferraris, A. Zakhidov, Z. Mansurov, Z. Bakenov and A. Ng, *J. Energy Storage*, 2024, **78**, 110035.

19 N. Chen, L. Ni, J. Zhou, G. Zhu, Q. Kang, Y. Zhang, S. Chen, W. Zhou, C. Lu and J. Chen, *ACS Appl. Energy Mater.*, 2018, **1**, 5189–5197.

20 Q. Lu, J. G. Chen and J. Q. Xiao, *Angew. Chem., Int. Ed.*, 2013, **52**, 1882–1889.

21 T. Liu, L. Finn, M. Yu, H. Wang, T. Zhai, X. Lu, Y. Tong and Y. Li, *Nano Lett.*, 2014, **14**, 2522–2527.

22 I. Shown, A. Ganguly, L. Chen and K. Chen, *Energy Sci. Eng.*, 2015, **3**, 2–26.

23 S. Malekpour, K. J. Balkus and J. P. Ferraris, *Nanotechnology*, 2021, **32**, 325401.

24 A. T. Brown, V. S. Agrawal, M. A. Wunch, J. Lin, M. C. Thomas, J. P. Ferraris, Y. J. Chabal and K. J. Balkus Jr, *ACS Appl. Energy Mater*, 2021, **4**, 12499–12507.

25 S. Bhoyate, P. K. Kahol, B. Sapkota, S. R. Mishra, F. Perez and R. M. Gupta, *Surf. Coat. Technol.*, 2018, **345**, 113–122.

26 I. Shaukat, N. Iqbal, T. Noor, M. Raza and R. Ahmad, *Energy Fuels*, 2023, **37**, 16150–16159.

27 S. Liu, L. Kang, J. Hu, E. Jung, J. Zhang, S. C. Jun and Y. Yamauchi, *ACS Energy Lett.*, 2021, **6**, 3011–3019.

28 Y. Yan, J. Lin, T. Xu, B. Liu, K. Huang, L. Qiao, S. Liu, J. Cao, S. C. Jun, Y. Yamauchi and J. Qi, *Adv. Energy Mater.*, 2022, **12**, 2200434.

29 Y. Tian, M. Abbas, S. F. Bin Haque, X. Zhu, J. P. Ferraris and K. J. Balkus Jr, *Next Mater.*, 2024, **3**, 100112.

30 T. Kshetri, D. T. Tran, D. C. Nguyen, N. H. Kim, K. Lau and J. H. Lee, *Chem. Eng. J.*, 2020, **380**, 122543.

31 R. Ahmad, N. Iqbal, T. Noor, S. K. Nemani, L. Zhu and B. Anasori, *ACS Appl. Nano Mater.*, 2024, **7**, 253–266.

32 R. Ahmad, N. Iqbal and T. Noor, *Materials*, 2019, **12**, 2940.

33 U. A. Khan, N. Iqbal, T. Noor, R. Ahmad, A. Ahmad, J. Gao, Z. Amjad and A. Wahab, *J. Energy Storage*, 2021, **41**, 102999.

34 M. A. Raza, A. Wahab, A. H. U. Bhatti, A. Ahmad, R. Ahmad, N. Iqbal and G. Ali, *Electrochim. Acta*, 2022, **407**, 139914.

35 Y. Tian, M. Abbas, S. F. Bin Haque, S. Tian, X. Zhu, G. Xiong, J. P. Ferraris and K. J. Balkus Jr, *ACS Appl. Nano Mater.*, 2023, **6**, 22720–22729.

36 B. E. Conway, *Electrochemical supercapacitors: scientific fundamentals and technological applications*, Springer Science & Business Media, 2013.

37 M. Okubo, A. Sugahara, S. Kajiyama and A. Yamada, *Acc. Chem. Res.*, 2018, **51**, 591–599.

38 M. Abbas, S. F. Bin Haque, Y. Tian, J. P. Ferraris and K. J. Balkus Jr, *Hybrid Nanomaterials: Biomedical, Environmental and Energy Applications*, Springer, 2022, pp. 359–383.

39 S. Saha, K. Arole, M. Radovic, J. L. Lutkenhaus and M. J. Green, *Nanoscale*, 2021, **13**, 16543–16553.

40 J. C. Varela, K. Sankar, A. Hino, X. Lin, W. Chang, D. Coker and M. Grinstaff, *Chem. Commun.*, 2018, **54**, 5590–5593.

41 Y. Yan, J. Lin, K. Huang, X. Zheng, L. Qiao, S. Liu, J. Cao, S. C. Jun, Y. Yamauchi and J. Qi, *J. Am. Chem. Soc.*, 2023, **145**, 24218–24229.

42 J. S. Shaikh, R. C. Pawar, A. V. Moholkar, J. H. Kim and P. S. Patil, *Appl. Surf. Sci.*, 2011, **257**, 4389–4397.

43 S. J. Patil, R. B. Pujari, T.-F. Hou and D.-W. Lee, *New J. Chem.*, 2020, **44**, 18489–18495.

44 S. Xiong, S. Jiang, J. Wang, H. Lin, M. Lin, S. Weng, S. Liu, Y. Jiao, Y. Xu and J. Chen, *Electrochim. Acta*, 2020, **340**, 135956.

45 H. Wang, M. Wang and Y. Tang, *Energy Storage Mater.*, 2018, **13**, 1–7.

46 A. Zakharov, A. Tukesheva, S. F. Bin Haque, J. Ferraris, A. Zakhidov, T. Tazhibayeva, T. Bazarbayeva and V. Pavlenko, *B. Univ. Karaganda – Phys.*, 2023, **111**, 16–33.

47 M. Singh Yadav, N. Singh and S. M. Bobade, *Mater. Today Proc.*, 2020, **28**, 366–374.

48 Y. N. Sudhakar, H. Hemant, S. S. Nitinkumar, P. Poornesh and M. Selvakumar, *Ionics*, 2017, **23**, 1267–1276.

49 K. K. Purushothaman, B. Saravanakumar, I. M. Babu, B. Sethuraman and G. Muralidharan, *RSC Adv.*, 2014, **4**, 23485–23491.

50 Z. Tian, H. Dou, B. Zhang, W. Fan and X. Wang, *Electrochim. Acta*, 2017, **237**, 109–118.

51 H. Chen, X. Q. Qi, M. Kuang, F. Dong and Y. X. Zhang, *Electrochim. Acta*, 2016, **212**, 671–677.

52 S. Katuwal, N.-A.-S. Rafsan, A. J. Ashworth and P. Kolar, *BioResources*, 2023, **18**, 3961.

53 D. G. Wang, Z. Liang, S. Gao, C. Qu and R. Zou, *Coord. Chem. Rev.*, 2020, **404**, 213093.

54 W. K. Cosey, K. J. Balkus Jr, J. P. Ferraris and I. H. Musselman, *Ind. Eng. Chem. Res.*, 2021, **60**, 9962–9970.

55 H. Furukawa, J. Kim, K. E. Plass and O. M. Yaghi, *J. Am. Chem. Soc.*, 2006, **128**, 8398–8399.

56 M. Tajik, S. F. Bin Haque, E. V. Perez, J. P. Vizuet, H. R. Firouzi, K. J. Balkus Jr, I. H. Musselman and J. P. Ferraris, *Nanomaterials*, 2023, **13**, 2291.

57 J. Jagiello, J. Kenvin, A. Celzard and V. Fierro, *Carbon*, 2019, **144**, 206–215.

58 H. Richter, H. Voss, N. Kaltenborn, S. Kämnitz, A. Wollbrink, A. Feldhoff, J. Caro, S. Roitsch and I. Voigt, *Angew. Chem., Int. Ed.*, 2017, **56**, 7760–7763.

59 M. Fernández-Arias, M. Boutinguiza, J. del Val, A. Riveiro, D. Rodríguez, F. Arias-González, J. Gil and J. Pou, *Nanomaterials*, 2020, **10**, 300.

60 Y. Zhai, Y. Ji, G. Wang, Y. Zhu, H. Liu, Z. Zhong and F. Su, *RSC Adv.*, 2015, **5**, 73011–73019.

61 C. Wan, Y. Jiao and J. Li, *J. Mater. Chem. A*, 2017, **5**, 17267–17278.

62 Z. Zhang and P. Wang, *J. Mater. Chem.*, 2012, **22**, 2456–2464.

63 T. A. O. Zheng and J. R. Dahn, *Carbon Mater. Adv. Technol.*, 1999, 341–388.

64 P. Bairi, S. Maji, J. P. Hill, J. H. Kim, K. Ariga and L. K. Shrestha, *J. Mater. Chem. A*, 2019, **7**, 12654–12660.

65 Y. Tian, X. Zhu, M. Abbas, D. W. Tague, M. A. Wunch, J. P. Ferraris and K. J. Balkus, *ACS Appl. Energy Mater.*, 2022, **5**, 6805–6813.

66 A. C. Ferrari and J. Robertson, *Phys. Rev. B: Condens. Matter Mater. Phys.*, 2000, **61**, 14095.

67 J. Schwan, S. Ulrich, V. Batori, H. Ehrhardt and S. R. P. Silva, *J. Appl. Phys.*, 1996, **80**, 440–447.

68 S. Bhaviripudi, X. Jia, M. S. Dresselhaus and J. Kong, *Nano Lett.*, 2010, **10**, 4128–4133.

69 X. Li, W. Cai, J. An, S. Kim, J. Nah, D. Yang, R. Piner, A. Velamakanni, I. Jung and E. Tutuc, *Science*, 2009, **324**, 1312–1314.

70 Z. Zhang and P. Wang, *J. Mater. Chem.*, 2012, **22**, 2456–2464.

71 A. N. Mansour, *Surf. Sci. Spectra*, 1994, **3**, 202–210.

72 C.-K. Wu, M. Yin, S. O'Brien and J. T. Koberstein, *Chem. Mater.*, 2006, **18**, 6054–6058.

73 S. D. Panangala, C. Karunaweera, R. Jayawickramage, K. J. Balkus Jr and J. P. Ferraris, *ACS Appl. Polym. Mater.*, 2019, **1**, 3203–3209.

74 H. Wang, H. Wang, F. Ruan, Q. Feng, Y. Wei and J. Fang, *Mater. Chem. Phys.*, 2023, **293**, 126896.

75 E. Samuel, H. S. Jo, B. Joshi, H. G. Park, Y. Il Kim, S. An, M. T. Swihart, J. M. Yun, K. H. Kim and S. S. Yoon, *Appl. Surf. Sci.*, 2017, **423**, 210–218.

76 F. Béguin, V. Presser, A. Balducci and E. Frackowiak, *Adv. Mater.*, 2014, **26**, 2219–2251.

77 D. Hernandez, C. R. Cabrera, L. Mendez, M. Diaz-Serrano, O. Vega, B. R. Weiner and L. G. Rosa, *Appl. Surf. Sci.*, 2015, **346**, 415–422.

78 J. Wang, M. Rao, C. Ye, Y. Qiu, W. Su, S. R. Zheng, J. Fan, S. L. Cai and W. G. Zhang, *RSC Adv.*, 2020, **10**, 4621–4629.

79 L. E. Helseth, *J. Energy Storage*, 2021, **35**, 102304.

80 J. H. Han, H. W. Kang and W. Lee, *Composites, Part B*, 2019, **178**, 107464.

81 K. Samdhyan, P. Chand, H. Anand and S. Saini, *J. Energy Storage*, 2022, **46**, 103886.

82 Y. Gong, R. Chen, H. Xu, C. Yu, X. Zhao, Y. Sun, Z. Hui, J. Zhou, J. An and Z. Du, *Nanoscale*, 2019, **11**, 2492–2500.

83 Q. Li, M. Wu, J. Zhao, Q. Lü, L. Han and R. Liu, *J. Electron. Mater.*, 2019, **48**, 3050–3058.

84 S. Zhao, H. Wu, Y. Li, Q. Li, J. Zhou, X. Yu, H. Chen, K. Tao and L. Han, *Inorg. Chem. Front.*, 2019, **6**, 1824–1830.

85 Y. Li, G. Zhu, H. Huang, M. Xu, T. Lu and L. Pan, *J. Mater. Chem. A*, 2019, **7**, 9040–9050.

86 F. Meng, Z. Fang, Z. Li, W. Xu, M. Wang, Y. Liu, J. Zhang, W. Wang, D. Zhao and X. Guo, *J. Mater. Chem. A*, 2013, **1**, 7235–7241.

87 B. K. Singh, A. Shaikh, R. O. Dusane and S. Parida, *J. Energy Storage*, 2020, **31**, 101631.

88 M. Singh, A. Gupta, P. Saharan, C. Kumar, S. Sundriyal, R. Padhye, T. Daeneke, N. R. Choudhary and S. R. Dhakate, *J. Energy Storage*, 2023, **67**, 107617.

89 L. Yaqoob, T. Noor and N. Iqbal, *Int. J. Energy Res.*, 2022, **46**, 3939–3982.